https://doi.org/10.1016/j.engstruct.2022.115263

Damage-Control Design and Hybrid Tests of a Full-Scale Two-Story Buckling-Restrained Braced Steel Moment Frame with Sliding Gusset Connections

Junxian Zhao[1,2], Lijian Yan[2], Chen Wang[3,*], Yun Zhou[4], Ruobing Chen[2], Tak-Ming Chan[3]

[1]State Key Laboratory of Subtropical Building Science, South China University of Technology, Guangzhou, China
[2]School of Civil Engineering and Transportation, South China University of Technology, Guangzhou, China
[3]Department of Civil and Environmental Engineering, The Hong Kong Polytechnic University, Hong Kong, China
[4]School of Civil Engineering, Guangzhou University, Guangzhou 510006, China

Abstract

Buckling-restrained braces (BRBs) are widely adopted as supplementary energy dissipation devices in steel moment frames (MFs) in Asia to improve the energy dissipation capacity of the whole system. Such systems are referred to as buckling-restrained braced moment frames (BRB-MFs). Nevertheless, adopting BRBs does not guarantee desirable seismic performance of the whole system, as frame action may cause premature fracture or buckling of BRB corner gusset connections, and such frame-to-gusset interaction may limit the ductility of such system. In our previous studies, a sliding corner gusset connection was proposed and proved to be able to substantially reduce the detrimental frame action at the connection level. In this paper, study was extended to (1) damage-control design of BRB-MFs with such connections in pursuit of enhanced system ductility, and (2) experimental evaluation on seismic behavior of BRB-MFs with such connections at the system level. The damage-control design method was first presented and a full-scale two-story BRB-MF designed by such procedure was experimentally studied under four levels of earthquake loading through hybrid tests, followed by a pseudo-static test to examine its failure mode. Test results showed that the sliding gusset connections effectively released the frame action at the system level. By adopting the damage-control design procedure, the test BRB-MF exhibited excellent seismic performance up to an inter-story drift ratio of ±3%, and plastic hinges of the MFs developed in the controlled positions without fracture or buckling under four levels of earthquake loading. With the improved ductility of MFs, BRBs achieved their full potential as energy dissipation devices.

Keywords: damage control, full-scale hybrid test, buckling-restrained brace, steel moment frame, sliding gusset connection

1 Introduction

Various techniques have been proposed and studied in recent years with the objective of achieving earthquake resistant structural systems (e.g., [1-13]). Among these techniques, buckling-restrained braces (BRBs) have been widely adopted owning to their stable behavior, superior energy dissipation capacity and excellent ductility under earthquake loading. Adopting BRBs in steel moment-resisting frames has been proven effective to improve the lateral stiffness and energy dissipation of the whole system. In this study, such systems are referred to as buckling-restrained braced moment frames (BRB-MFs). Compared to the relatively flexible pure moment frames, the lateral drifts of BRB-MFs under earthquake loadings can be easily controlled to be within a specified limit. As such, BRB-MFs have gained wide acceptance within the engineer community, especially in Asia (China,

* Corresponding author (Chen Wang), Ph.D., E-mail: chen2.wang@polyu.edu.hk

Japan, etc.) where moment-resisting beam-to-column connections are typically required by design codes [14,15] to meet the minimum structural lateral stiffness demand and to provide possible structural redundancy. However, adopting BRBs does not necessarily guarantee satisfactory seismic performance of BRB-MFs for a few reasons.

Firstly, at the connection level, gusset plates, which are usually welded to the beam and column flanges, are typically used to connect BRBs with the frame to transfer the brace action force. It was found that the frame action (i.e. opening and closing behavior of the beam-column joint) under strong earthquake loading would impose significant forces on the gusset plates due to the strong frame-to-gusset interaction (see Figure 1) [16-18]. Particularly, the shear interaction at the gusset-to-frame interfaces induced from elongation and shortening of the beam/column flanges was found to be the major source for frame action force. As such, premature rupture or instability in gusset plate connections have been frequently witnessed in previous experimental tests [18-23], which prevented BRBs to fulfill their function. Although the early failure in the BRB connection region may not necessarily occur, the early failures frequently witnessed in the previous tests indicate there is possibility that the frame action may cause early failure in the BRB connection region if it is not dealt with properly.

Secondly, at the system level, it was found that the frame action force may cause the MF to fail by premature local buckling and rupture of beams or columns near the gusset plate [23]. This will prevent BRBs from fulfilling their potential and the performance of the whole BRB-MF under strong earthquakes will be substantially deteriorated. Therefore, compatible deformation of the MF part of BRB-MFs is required to accommodate the deformation of BRBs.

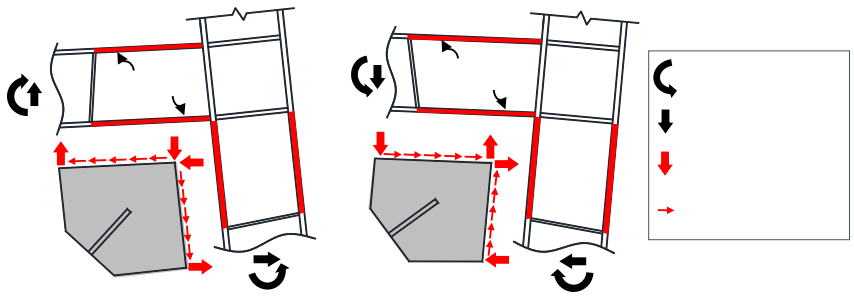

(a) (b)

Figure 1 Frame action: (a) Joint opening; (b) Joint closing

To minimize the negative frame action effect, the first author proposed a novel sliding gusset connection [24], whose components, assembly process, and sliding mechanism are illustrated in Figure 2. The gusset plate is

first welded to an L-shaped end plate which is sandwiched by shim plates and the beam/column flanges through pretensioned high-strength bolts. Low-frictional butyl rubber layers are adopted at the end plate-to-flange interface and the shim plate-to-end plate interface to facilitate sliding at these interfaces. Slotted bolt holes are used in the end plate to exempt the bolts from bearing against the bolt holes during the sliding process. The low-frictional sliding can essentially release the shear restraint at the gusset-to-frame interfaces and therefore substantially reduce the detrimental frame action effect. In such a way, reliable BRB-to-frame connection performance is more achievable.

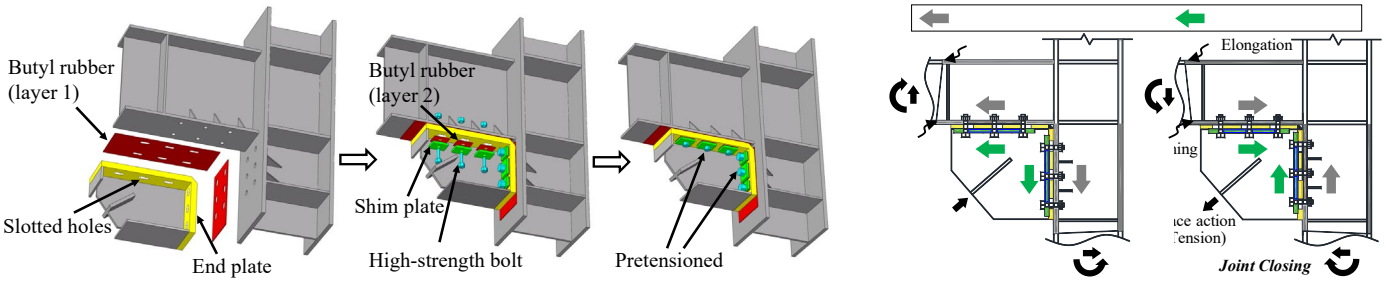

Figure 2 Sliding gusset connection: (a) assembly of components; (b) sliding mechanism

A series of experimental tests and finite element (FE) analyses by the authors [24,25] showed that as compared to the conventional connection with gusset plate welded directly to beam and column flanges (Figure 1), the sliding gusset connection is effective in reducing the detrimental frame action effect without compromising the energy dissipation capacity of BRBs, and a practical design procedure was established for the sliding gusset connections. However, these previous studies are limited to the connection level, with the focus on characterizing the behavior of the sliding gusset connection only. It still remains unclear how to conduct the system design to achieve the aforementioned compatible deformation between the MF and BRBs when the sliding gusset connections are provided, specifically, what is the preferred failure hierarchy of the system and how to arrange the strengths of individual components accordingly.

In this paper, a full-scale two-story BRB-MF with sliding gusset connections was designed and fabricated for a prototype building. Firstly, with the aim of attaining compatible lateral deformation capacity between the MF and BRBs, the damage-control design concept was practiced in the design of the test BRB-MF. Subsequently, pseudo dynamic hybrid testing of the BRB-MF was conducted subjecting to earthquake ground motions

corresponding to four seismic hazard levels, following which pseudo static loading was continued until the system failed. The main objectives of this study include: (1) to evaluate the proposed damage-control design procedure on its effectiveness to attain compatible deformation capacity between the MF and BRBs in the BRB-MF system with sliding gusset connections; (2) at the system level, to evaluate the effectiveness of the practical design procedure for the sliding gusset connections proposed in the authors' previous study [25]; (3) at the system level, to study the behavior of the sliding gusset connections and its effect on the MF in the context of a realistic braced frame (including the effect of the composite floor slabs).

2 Prototype building

In view of the height limit and loading capacity of the structural laboratory, the full-scale test BRB-MF was set to be two-story. The prototype office building located in Beijing, China was designed to provide a realistic context. Its plan view and the position of the test BRB-MF are shown in Figure 3(a).

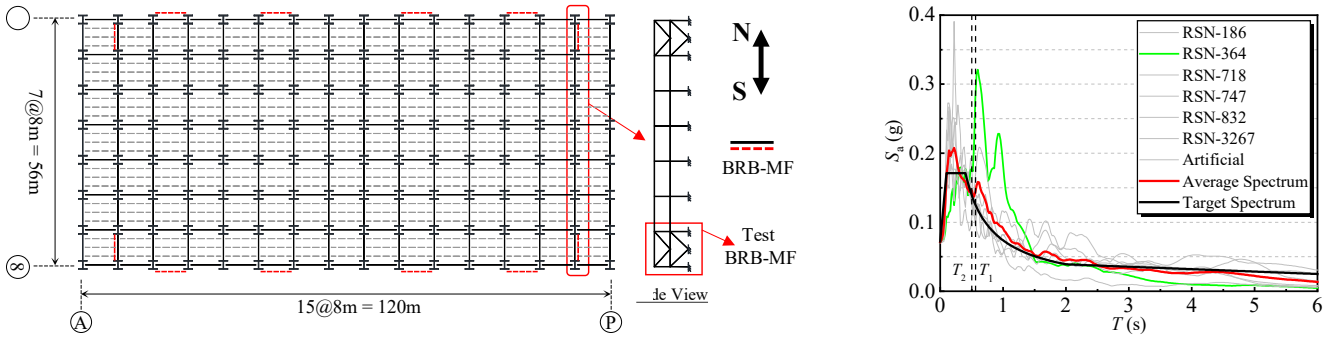

Figure 3 (a) Plan view of prototype building; (b) Response spectra of ground motions and the design response spectrum

In accordance with China's Code for Seismic Design of Buildings [14], the seismic design parameters for this building are: 8-degree seismic precautionary intensity, site class II, and the second design earthquake group. The corresponding design basic acceleration of ground motion (with the exceedance probability of 10% in 50 years) is 0.2g and the site characteristic period is 0.4 s. The dead load, D, was taken as the self weight of the structure plus 2.0 kN/m^2, and the live load, L, was taken as 2.0 kN/m^2. The load combination involving the earthquake action (denoted as E) was 1.3E+1.2D. The seismic weights were 46668 and 41983 kN at the first and second floor, respectively, as determined by the load combination 1.0D+0.5L.

Two phases of design were conducted in accordance with the Chinese Code for Seismic Design of Buildings (GB 50011-2010) [14]. In Design Phase 1, the prototype building was designed to remain elastic under the design seismic load corresponding to the frequently occurring earthquake (FOE, with an exceedance probability of 63% in 50 years). The inter-story drift ratios (IDRs) corresponding to Design Phase 1 is required to be no larger than 0.4%. In Design Phase 2, preliminary nonlinear time history analyses were conducted using OpenSees [26] subjected to rare earthquakes (RE) with an exceedance probability of 2% in 50 years. According to GB 50011-2010, in Design Phase 2, at least seven earthquake ground motion records shall be used, and the design requirement is that the average of maximum IDRs under the seven ground motions shall be no greater than 2%. Among the seven ground motions, six were from the PEER Ground Motion Database [27] whose information is presented in Table 1, and one was artificially simulated. All the selected ground motions were scaled to have the PGA of 400 cm/s^2 to represent the RE hazard level according to GB 50011-2010 [14]. The 5% damped response spectra of the seven ground motions and the target design response spectrum are compared in Figure 3(b). Among the seven ground motion records, the one that has the largest response spectral accelerations at the periods of the first two natural periods of the building structure was selected for the hybrid tests presented in Section 4.3, specifically, the RSN-364 record from the earthquake Coalinga-01.

According to previous studies, damping typically increases with the amplitude of structural response, which is believed to be attributed to the more severe damage of structural and non-structural elements, the higher level of friction between different components, etc. [28]. In the Chinese Code for Seismic Design of Buildings (GB 50011-2010) [14], the damping ratio of 4% and 5% are recommended for steel structures under FOE-level earthquakes and RE-level earthquakes, respectively. Damping ratios consistent with the recommended values were adopted in the design of the prototype building. The structural design results for the prototype building are summarized in Table 2.

Table 1 Ground motion records for structural design of the prototype building

Record Sequence Number	Event Name	Year	Station Name	Magnitude	Fault Type

186	Imperial Valley-06	1979	Niland Fire Station	6.53	Strike Slip
364	Coalinga-01	1983	Parkfield - Vineyard Cany 4W	6.36	Reverse
718	Superstition Hills-01	1987	Wildlife Liquef. Array	6.22	Strike Slip
747	Loma Prieta	1989	Bear Valley #7, Pinnacles	6.93	Reverse Oblique
832	Landers	1992	Amboy	7.28	Strike Slip
3267	Chi-Chi, Taiwan-06	1999	CHY027	6.3	Reverse

Table 2 Structural design results of the prototype building

Structural Member	Steel Grade	Section
Columns in BRB-MF	Grade Q345-B	H400×400×13×21
Other columns	Grade Q345-B	H350×350×12×19
Main beams	Grade Q235-B	H488×300×11×18
Secondary beams	Grade Q235-B	H400×200×8×13
BRB in 1st story	Grade Q235-B	Design yield strengths (P_y) = 700 kN
BRB in 2nd story	Grade Q235-B	Design yield strengths (P_y) = 300 kN

3 Damage-control design of the test BRB-MF

3.1 Performance objectives

As discussed in the Introduction, the ductility of the MF in the BRB-MF system should be comparable with that of the BRBs to ensure a compatible working relationship under strong earthquakes. As compared to the conventional design of pure MF system, the addition of BRB force and the unique force transfer behavior between the frame and the sliding gusset connections impose more challenges to design of the BRB-MF system. To achieve the required system-level ductility under strong earthquakes, performance objectives (POs) for each part of the BRB-MF system with sliding gusset connections are determined as follows:

PO 1: Sliding gusset connections should remain elastic under the expected maximum BRB forces to ensure reliable force transfer between BRBs and the MF.

PO 2: Unlike the plasticity distribution in pure MF system, beam plastic hinges in the BRB-MF should be controlled to be specifically located outside the sliding gusset connection regions to minimize the frame-to-gusset normal interaction, as indicated in the previous study [25].

PO 3: In addition to the shear force demand from moment frame action, beams and columns within the sliding gusset connection region should be able to resist the shear force demand arising from the connecting BRB action.

PO 4: Instead of allowing plastic deformation in panel zones in conventional MFs, the panel zones in BRB-MFs should remain elastic to minimize the shear deformation, so as to reduce the frame-to-gusset normal interaction, as indicated in the previous study [25].

PO 5: By considering the influence of BRB force, plastic hinges of the frame should be controlled to be in beams and column feet to achieve the preferable beam sidesway mechanism.

PO 6: Local buckling at the expected plastic hinges of the frame should be minimized, if not eliminated, to achieve sufficient rotation capacity under the expected maximum lateral drift.

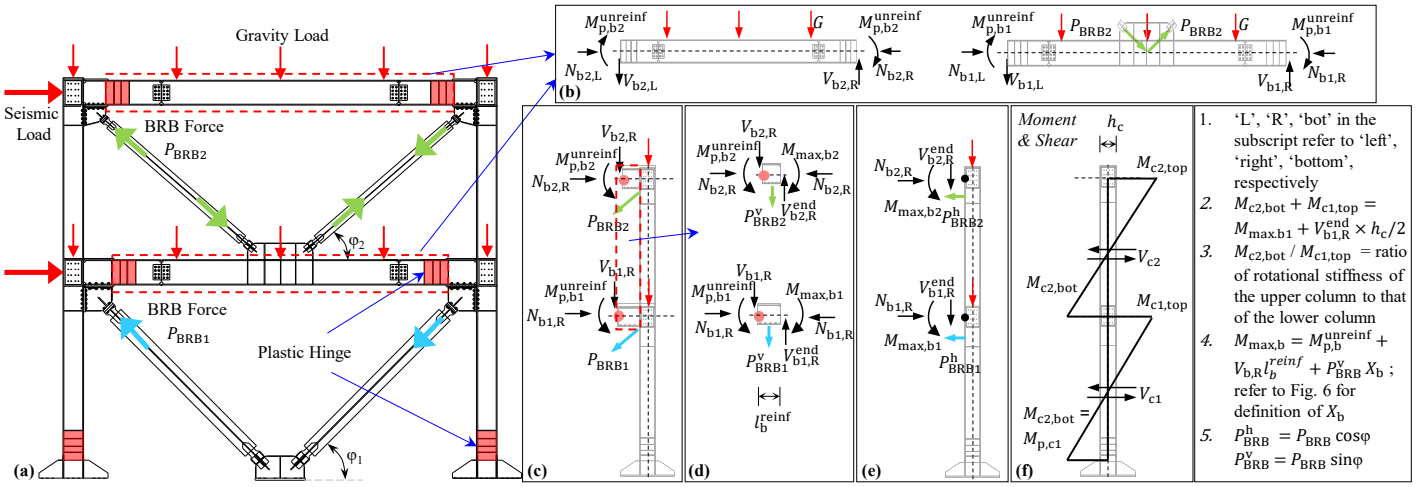

Figure 4 Assumed response of the BRB-MF under extreme loading

To accomplish the specified performance objectives, damage control design procedures were proposed and practiced in design of the test BRB-MF, which are elaborated in the following sections. Under extreme loading condition, it is assumed that all BRBs have reached their ultimate strengths and plastic hinges have developed in the intended positions (highlighted in red color in Figure 4(a)). The calculation of internal forces is illustrated in Figure 4(b)-(f). Figure 4(b) shows the free body diagrams of beams. With the assumption that plastic hinges form at the intended positions and BRBs reach their capacity, the internal forces at beam ends can be calculated through equilibrium and they will be transferred to the columns. Through the equilibrium of the free bodies shown in

Figure 4(c) to (e), the moment and shear force distribution of the columns can be obtained as shown in Figure 4(f), which is used to determine the critical strength demand for columns.

3.2 Design of sliding gusset connections (PO 1)

The design procedure developed in Zhao et al. [25] was followed. Firstly, the expected maximum strength of the BRB, P_{BRB}, can be calculated as

$$P_{\mathrm{BRB}} = 1.5 \times P_{\mathrm{y}} \tag{1}$$

where P_{y} is the design yield strength of the BRB, and 1.5 is the factor to account for the strain hardening of the core plate with a steel grade of Q235 and the friction between the core plate and the restrainer.

The previous study [25] revealed that, when BRBs are loaded in tension, the force is mainly transferred through tension loading of the bolt groups at the sliding gusset-to-frame interfaces, as shown in Figure 5(a). The acting points of the equivalent tensile forces can be determined as:

$$X_{\mathrm{b}} = 0.3\left(L_{\mathrm{b}} - t_{\mathrm{pc}}\right)\left(1 + \sqrt{d_{\mathrm{c}}/d_{\mathrm{b}}}\right)^{0.6} + t_{\mathrm{pc}} \tag{2}$$

$$X_{\mathrm{c}} = \left(e_{\mathrm{c}} + X_{\mathrm{b}}\right)\tan\varphi - \left(e_{\mathrm{b}} + t_{\mathrm{p}}\right) \tag{3}$$

where d_{c} and d_{b} are the distance between the BRB axis and the effective weld centroids on the column side and the beam side, respectively. To ensure elasticity in the bolts and to minimize the axial deformation loss of BRB under brace tension, the bolts were designed based on the criterion:

$$N_{\mathrm{t}} \le 0.8P_{\mathrm{bolt}} \tag{4}$$

where N_{t} is the critical tensile force demand and P_{bolt} is the prescribed bolt pretention force.

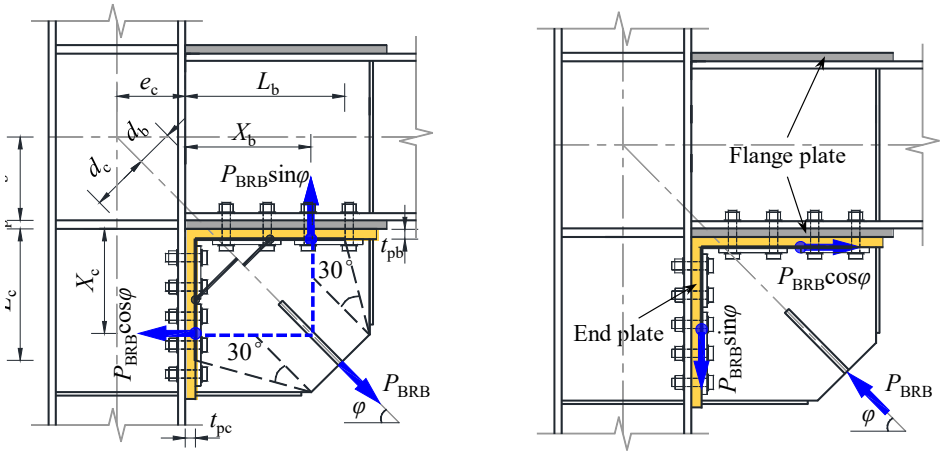

(a) (b)

Figure 5 Assumed force transfer at sliding gusset connection: (a) brace tension, (b) brace compression

Under the compressive BRB loading, sliding gusset connections were proved to work in a similar way as conventional welded gusset connections. The design method, which assumes that the vertical ($P_{\mathrm{BRB}}\sin\varphi$) and horizontal ($P_{\mathrm{BRB}}\cos\varphi$) components of the compression brace force are transferred through the gusset-to-column and gusset-to-beam paths, respectively (Figure 5(b)), was adopted [29]. The ratio of the shear stress demand to the nominal shear yield strength of gusset plate, τ/f_{vy}, was controlled to be less than 0.7 following the previous study [25].

3.3 Control of beam plastic hinge location (PO 2)

The flange plate configuration (see Figure 5), in which two steel plates are added to connect the upper and lower beam flanges to the column, was adopted to strengthen the beam end. The flange plates were connected to beam flanges through fillet welds and to the column flange through complete penetration welds as shown in Figure 6. To shift the beam plastic hinges outside the gusset region, the flange plates covered the entire gusset connection region and extended by another 50 mm. The effect of the composite floor on the strengths of beams was ignored.

As the first step, the moment capacity of the unreinforced beam section, $M_{\mathrm{p,b}}^{\mathrm{unreinf}}$, is determined. In this study, an axial force in the beam equal to the horizontal component of P_{BRB} of the BRB below was considered in the calculation of $M_{\mathrm{p,b}}^{\mathrm{unreinf}}$ to avoid overestimation, which is well defined in related codes [30]. Other internal forces can be calculated through the equilibrium analysis of different free bodies as illustrated in Figure 4. To attain the elasticity of the reinforced beam end, the following strength criterion was checked to be satisfied:

$$\frac{M_{\mathrm{max,b}}}{M_{\mathrm{y,b}}^{\mathrm{reinf}}}+\frac{N_{\mathrm{b}}}{N_{\mathrm{y,b}}^{\mathrm{reinf}}}<1 \tag{5}$$

where $M_{\mathrm{y,b}}^{\mathrm{reinf}}$ and $N_{\mathrm{y,b}}^{\mathrm{reinf}}$ are the nominal yield moment strength and the nominal yield tensile strength of the reinforced beam end section, respectively.

3.4 Shear yielding capacity control of beams and columns (PO 3)

In BRB-MFs, both the moment frame action and BRBs will introduce shear force to frame members (Figure 4(d)). To ensure reliable shear force transfer, the nominal shear strength of the reinforced beam end section ($V_{\mathrm{y,b}}^{\mathrm{reinf}}$) is designed to satisfy

$$V_{\mathrm{y,b}}^{\mathrm{reinf}} > V_{\mathrm{b}}^{\mathrm{end}} \quad (6)$$

where $V_{\mathrm{b}}^{\mathrm{end}}$ is the critical shear force demand of the beam end section. Similarly, columns are designed to satisfy

$$V_{\mathrm{y,c}} > V_{\mathrm{c,max}} \quad (7)$$

where $V_{\mathrm{y,c}}$ and $V_{\mathrm{c,max}}$ are the nominal shear strength and critical shear force demand of the column section.

3.5 Shear yielding capacity control of the panel zone (PO 4)

To achieve elastic panel zones, one strengthening plate was welded on the column web in each panel zone to satisfy

$$(\sum M_{\mathrm{max,b}})/V_{\mathrm{p}} \leq \frac{4}{3} f_{\mathrm{vy}} \quad (8)$$

where $\sum M_{\mathrm{max,b}}$ is the summation of the maximum moments that are transferred to the panel zone from the connecting beams, f_{vy} = nominal steel shear yield strength of the panel zone; V_{p} = effective volume of the panel zone. Unlike conventional design of MFs, the beam moment reduction factor was not considered to avoid plasticity in the panel zone.

3.6 Control of beam sidesway mechanism (PO 5)

To ensure that plastic hinges of the MF develop in beams rather than in columns (excluding column bases), the 'strong column-weak beam' principle was practiced for each beam-to-column joint by following

$$\sum M_{\mathrm{p,c}}\left(1 - N_{\mathrm{c}}/N_{\mathrm{y,c}}\right) \geq \sum M_{\mathrm{max,b}} \quad (9)$$

where $M_{\mathrm{p,c}}$ = the nominal plastic moment capacity of the column section, $N_{\mathrm{y,c}}$ = the nominal axial yield strength of the column, and N_{c} = the axial load in the column which can be calculated as the summation of all the above vertical loads. As shown in Figure 4, in addition to the gravity load, two other sources were considered in the calculation of the axial load in the column: (1) the vertical components of BRB forces assuming all BRBs reach their capacity, i.e., $P_{\mathrm{BRB}}^{\mathrm{v}}$; (2) the shear forces at beam ends assuming plastic hinges have formed at intended positions, i.e., $V_{\mathrm{b}}^{\mathrm{end}}$. As it is unlikely that the vertical loads transferred from beams at all stories reach their maximum simultaneously, the square root of the sum of square (SRSS) of the vertical load from the beams above was used to calculate the axial load in the column.

3.7 Seismic detailing of expected plastic hinges (PO 6)

To enhance the plastic rotational capacity of the expected plastic hinges (highlighted in red color in Figure 4(a)), transverse stiffeners were added at beam sections outside the gusset region along a length equal to the beam section height, and at column feet along a length equal to the column section height. Compared to the thickened beam flange and thickened column flange strategy, providing stiffeners was a more economic way to improve the ductility of the MFs. The spacing of transverse stiffeners was determined as 110-150 mm, which were derived from the theoretical inelastic buckling analysis of the flange plates that are simply supported on three sides and free on one side [31]. Effectiveness of the stiffener spacing was validated by finite element analysis of the test frame loaded to an IDR of 3%.

4 Pseudo dynamic hybrid test

4.1 Specimen

Table 3 Primary demand-to-capacity ratios (DCRs) of the test BRB-MF

Performance Objective	Design Criterion	DCR	
		1st story	2nd story
PO 1: sliding gusset connection	Eq. (4)	0.49 (beam side) 0.53 (column side)	0.32 (beam side) 0.59 (column side)
	τ/f_{vy}	0.46 (beam side) 0.53 (column side)	0.44 (beam side) 0.45 (column side)
PO 2: Beam plastic hinge location	Eq. (5)	0.73	0.68
PO 3: Frame shear capacity	Eq. (6) & (7)	0.82 (beam) 0.43 (column)	0.48 (beam) 0.4 (column)
PO 4: Panel zone	Eq. (8)	1.0 (interior column) 0.61 (side column)	0.99 (interior column) 0.55 (side column)
PO 5: Beam sidesway mechanism	Eq. (9)	0.87 (interior column) 0.51 (side column)	N.A.

Table 4 Material properties of steel components

Component	Steel Grade	Thickness /Diameter (mm)	Yield Strength (MPa)	Ultimate Strength (MPa)	Elongation (%)	Young's Modulus (GPa)	Poisson's Ratio
BRB1 Core plate	Q235-B	16	266	424	35	205	-
BRB2 Core plate	Q235-B	10	270	423	32	205	-
BRB1 gusset plate	Q345-B	16	366	516	28	202	0.28
BRB2 gusset plate	Q345-B	10	347	509	31	200	0.28
Beam flange	Q235-B	18	262	423	33	204	-
Beam web	Q235-B	11	335	448	23	204	-
Column flange	Q345-B	21	352	514	32	205	-
Column web	Q345-B	13	377	525	31	205	-
Steel rebar	HRB400	8	424	695	-	200	-

Figure 6 shows the labelling and details of structural components of the test BRB-MF, whose design was conducted following the damage-control design procedures elaborated in Section 3. All the high-strength bolts in the sliding gusset connections are of Grade 10.9 (minimum ultimate strength=1040MPa; yield strength/ultimate ratio=0.9). The lengths of the slotted bolt holes in the end plates were determined to accommodate the sliding demand corresponding to 2% elongation/shortening of the beam/column flanges within the gusset connection region. BRBs were connected with the gusset plates through welded steel angles at bottom ends and bolted end plates at top ends. The profiled steel decks were 1 mm thick with ribs parallel to the main beam, and their flutes were 50 mm deep and were spaced at 280 mm center to center. Two rows of shear studs (80 mm in height and 16 mm in diameter) were adopted on the main beam with spacing of 100 mm in the transverse directions. Based on the design criteria for each PO, the primary demand-to-capacity ratios (DCRs) of the test BRB-MF are listed in Table 3. The tension coupon tests were conducted to determine the actual properties of steel members. The results are listed in Table 4. The concrete strength test revealed that the cube compressive strength of the concrete in the floor slabs was 23 MPa on the day of testing.

To avoid difficulties in on-site assembly of the beam, column and sliding gusset connection, prior to being transported to the site, the short beam stubs were welded to the columns and the sliding gusset plates were bolt-connected to the beam stub and column in shop. After transported to the site, the beam-column-gusset subassemblies were erected first, and the middle beams were then connected to the beam stubs through bolted splice plates on the web and welding of beam flanges.

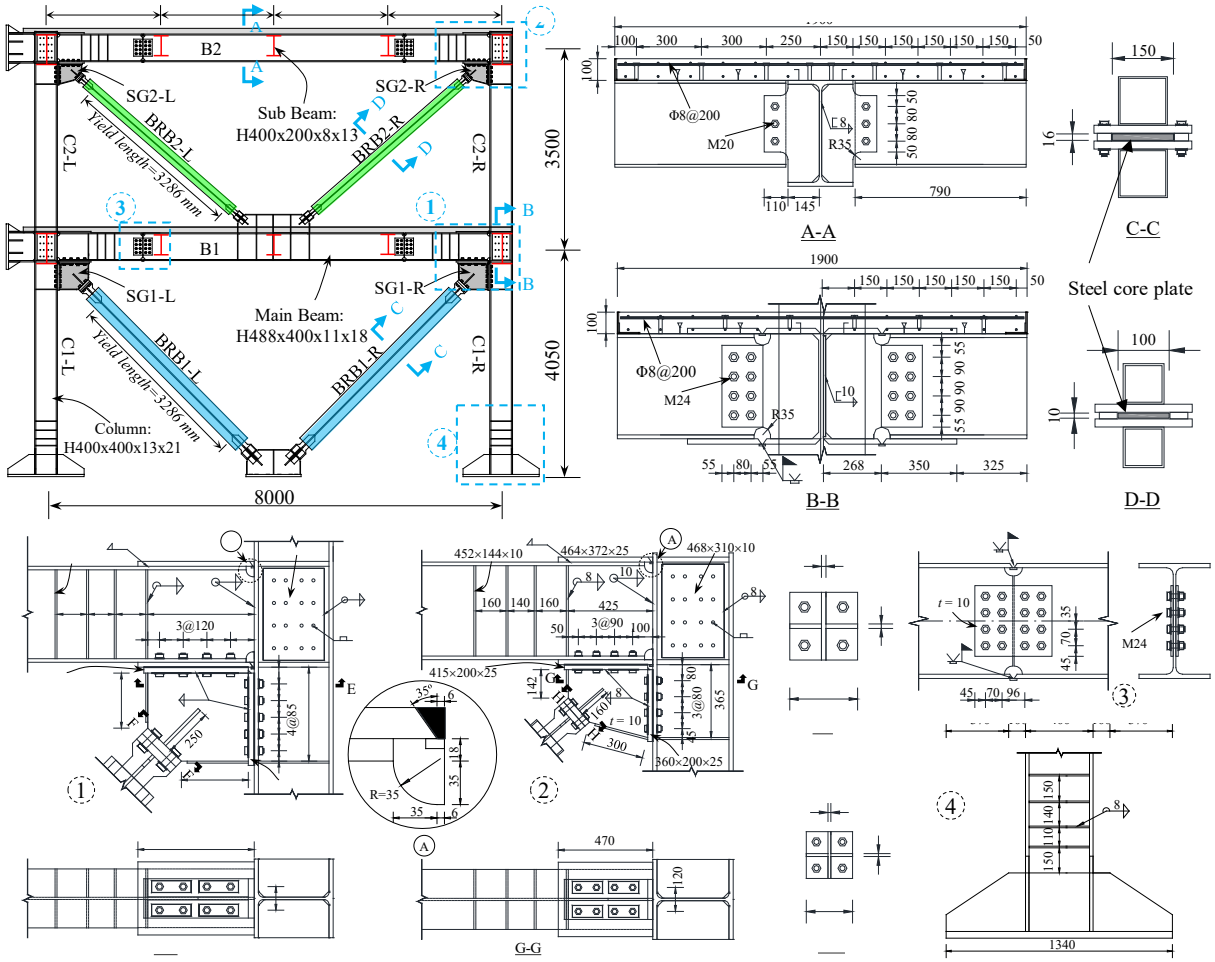

Figure 6 Labelling and details of structural components

4.2 Test setup and instrumentation

Figure 7 shows the test setup and instrumentation. The out-of-plane stability of the test frame was provided through lateral support using two pairs of rollers at each floor. The instrument layout (right half) and the strain gauge layout (left half) shall be interpreted in a way that either layout be mirrored about the symmetry plane to obtain the complete layout. Far right of Figure 7 are strain gauge arrangements at beam sections (denoted by SB1 and SB2) and column sections (denoted by SC1, SC2, and SC3). For each sliding gusset connection, two LVDTs were installed to measure the relative movement between the gusset plate tip and the nearest transverse stiffener on the beam and column. This relative movement corresponds to the sliding at the gusset-to-frame interfaces caused by both the rigid-body movement of the gusset plate and the axial deformation of the beam/column flange. Since the bolts near the gusset corner on the column side usually bear the largest tensile forces under brace tension

loading [25], four ring load cells were installed to measure the tensile forces of these bolts on the south side of the test frame.

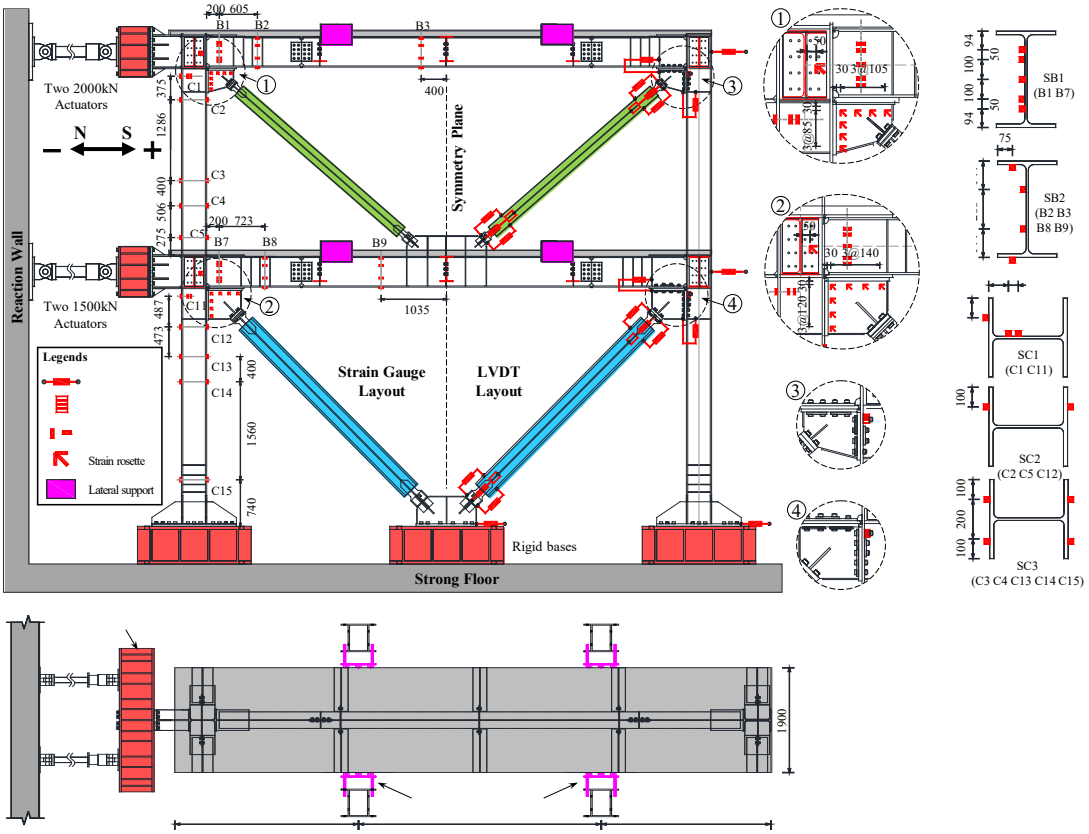

Figure 7 Test setup and instrumentation

4.3 Testing methodology and loading protocols

The pseudo dynamic hybrid testing and pseudo-static testing methods were adopted, respectively, to examine the seismic performance and ultimate failure modes of the test BRB-MF. Figure 8 illustrates the hybrid testing method. Part of the prototype structure was physically tested (i.e., the test BRB-MF in this study), referred to as the physical substructure, and the rest of the prototype structure was simultaneously numerically modelled, referred to as the numerical substructure. The numerical substructure was constructed in *OpenSees* [26]: the beams and columns were modeled using the displacement-based beam-column elements, with fiber-based sections replicating the geometry of the corresponding cross section; the truss elements using the *Steel02* material were used to model BRBs; beams were fix-connected with columns in the model to reflect the moment beam-to-column connections. The floor slabs and the panel zones were not considered in the model. Rigid diaphragms were

assumed by constraining the translational degrees of freedom of the nodes at each level. The earthquake loading was applied in the North-South direction and the torsion of the structure was not considered.

In the numerical substructure, the gravity load was applied to the nodes at each floor level and the values were determined based on the tributary area of each node. In the physical substructure, a floor slab of 1900 mm width was considered at each floor, but additional gravity load was not considered. Following the damage-control design method proposed in this paper, most of the strength demand of the frame comes from the earthquake load with all BRBs reaching their capacity. The strength demand from gravity load effect is relatively small. The neglection of the additional gravity load transferred from floor slab is therefore not expected to have a significant impact on the behavior of the frame. The earthquake loading was applied in the North-South direction and the torsion of the structure was not considered.

The hybrid test was controlled using the hybrid simulation platform named HyTest [32,33]. The whole structure was simplified as an equivalent two-DOF lumped-mass model, whose motion equation under the input earthquake ground motion ($\ddot{\boldsymbol{x}}_{\mathbf{g}}$) was constructed and solved in HyTest in the discretized form as:

$$\boldsymbol{M}\ddot{\boldsymbol{x}}_{\boldsymbol{i}} + \boldsymbol{C}\dot{\boldsymbol{x}}_{\boldsymbol{i}} + \boldsymbol{F}_{\mathbf{N}}(\boldsymbol{x}_{\boldsymbol{i}}) + \boldsymbol{F}_{\mathbf{P}}(\boldsymbol{x}_{\boldsymbol{i}}) = -\boldsymbol{M}\ddot{\boldsymbol{x}}_{\mathbf{g},\boldsymbol{i}} \quad (10)$$

where $\boldsymbol{F}_{\mathbf{N}}(\boldsymbol{x}_{\boldsymbol{i}})$ is the restoring force vector provided by the numerical substructure and $\boldsymbol{F}_{\mathbf{P}}(\boldsymbol{x}_{\boldsymbol{i}})$ is the restoring force vector provided by the physical substructure. During the hybrid test, at the time step i, $\boldsymbol{F}_{\mathbf{N}}(\boldsymbol{x}_{\boldsymbol{i}})$ is obtained by loading the numerical substructure model to the target lateral displacement, $\boldsymbol{x}_{\boldsymbol{i}}$, while $\boldsymbol{F}_{\mathbf{P}}(\boldsymbol{x}_{\boldsymbol{i}})$ is experimentally measured in the physical test under the target lateral displacement, $\boldsymbol{x}_{\boldsymbol{i}}$. Both $\boldsymbol{F}_{\mathbf{N}}(\boldsymbol{x}_{\boldsymbol{i}})$ and $\boldsymbol{F}_{\mathbf{P}}(\boldsymbol{x}_{\boldsymbol{i}})$ will be fed back to HyTest where the motion equation will then be solved to obtain the target lateral displacement for the next step, $\boldsymbol{x}_{\boldsymbol{i+1}}$. In this study only horizontal forces from the physical structure (measured from the actuators) can be fed back to HyTest to update the calculation. As noted in Eq. 10, the mass of the whole building (including both the numerical and physical substructures) is accounted for by the term $\boldsymbol{M}\ddot{\boldsymbol{x}}_{\boldsymbol{i}}$. The mass matrix of the physical substructure is not necessarily required, and the loading rate of the physical substructure was kept slow in the test to exclude the effect of the mass of the physical substructure. Moreover, as the restoring force, $\boldsymbol{F}_{\mathbf{P}}(\boldsymbol{x}_{\boldsymbol{i}})$, can be

directly obtained by measurement of forces in the test, the stiffness matrix of the physical substructure is also not required in this case.

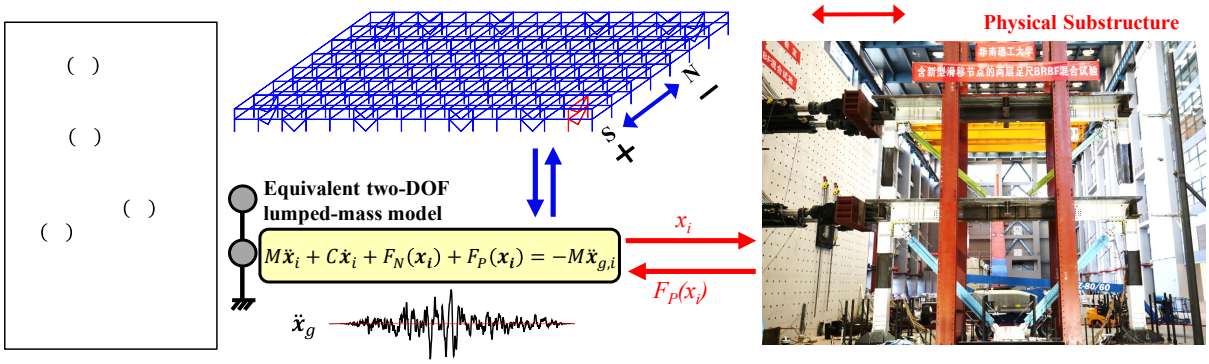

Figure 8 Pseudo dynamic hybrid test method

The RSN-364 ground motion record was scaled to have the peak ground accelerations (PGAs) of 0.07g, 0.2g, 0.4g, and 0.58g, corresponding to the hazard levels of frequently occurring earthquake (FOE), design basis earthquake (DBE), rare earthquake (RE), and very rare earthquake (VRE), respectively, as per [34], whose information is listed in Table 5. The time history of the ground motion scaled to the DBE level is shown in Figure 9(a). Four hybrid tests were conducted subjected to the four scaled ground motions sequentially with increasing seismic hazard, followed by a pseudo static test to examine the ultimate failure modes of the specimen, with the loading protocol shown in Figure 9(b). Consistent with the damping ratios adopted in the design of the prototype building, 4% and 5% were adopted for the FOE and RE level earthquake loading, respectively. For the DBE-level and the VRE-level loading, no damping ratios were recommended in the code [14], and the damping ratios of 4% and 5% were adopted, respectively, which is believed to be reasonable in this context as DBE-level is stronger than FOE-level and VRE-level is stronger than RE-level. The IDRs in the 1st story and 2nd story were controlled to be synchronized in the pseudo static test.

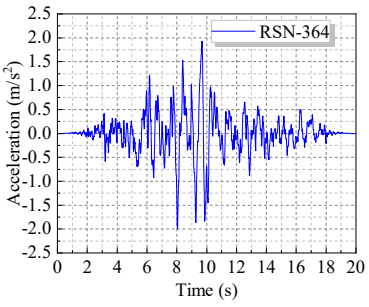

(a)

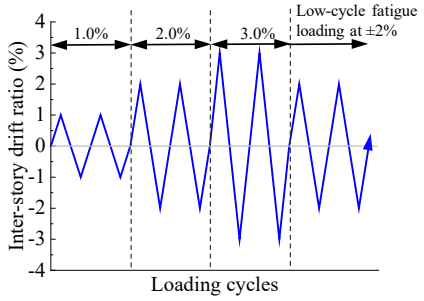

(b)

Figure 9 Loading history: (a) time history of DBE-level ground motion for hybrid test; (b) for pseudo static test

Table 5 Ground motion selection and scaling for the pseudo dynamic hybrid tests

Earthquake	Component	PGA (g)	Damping ratio	Hazard level (Exceedance probability)
Coalinga-01	H-VC4000	0.07	0.04	FOE (63% in 50 years)
		0.2	0.04	DBE (10% in 50 years)
		0.4	0.05	RE (2% in 50 years)
		0.58	0.05	VRE (10^{-4} per year)

5 Experimental results and discussion

5.1 Global response and limit state (LS) evolution

In the following discussion, lateral displacements are considered as positive when the frame moves in the south direction. The IDRs of the 1st and 2nd story, θ_1 and θ_2, are defined as the relative lateral displacement between the upper floor and lower floor divided by the corresponding story height. The 2nd story shear force, $V_{\text{BRB-MF,2}}$, was equal to the actuator force applied at the 2nd floor; the 1st story shear force, $V_{\text{BRB-MF,1}}$, was equal to the sum of the actuator forces applied at both the 1st and 2nd floors. The shear force in the i^{th} story, $V_{\text{BRB-MF,i}}$, is jointly resisted by columns ($V_{C,i}$) and BRBs ($V_{BRB,i}$). The horizontal shear force in the frame columns, $V_{C,i}$, can be derived through strain gauge data collected at column sections in the elastic regions. For instance, based on the strain gauge data, the moment at column sections C3 and C4 (shown in Figure 7) could be obtained first; the shear force in the column could subsequently determined by the difference in the moments of the two sections divided by the distance between the two sections. Figures 10 and 11 show the disaggregation of the story shear-IDR responses under different loading phases for the 1st and 2nd story, respectively. Positions and evolution of LSs are summarized in Figure 12.

Under the FOE-level loading, both the BRBs and the frame remained elastic, with the maximum IDRs of θ_1 = -0.2% and θ_2 = +0.18%, which satisfied the performance objective for the structure to remain elastic and for IDRs to be within the ±0.4% limit at this seismic hazard level.

Under the DBE-level loading, the BRBs in the 1st and the 2nd stories yielded at θ_1 = +0.23% and θ_2 = -0.23% (denoted as LS1), respectively, followed by slight yielding of the 1st story beam at θ_1 = +0.8% (denoted as LS2). Prior to the frame yielding, BRBs yielded significantly to dissipate the seismic energy, which followed the designed yielding hierarchy.

Under the RE-level loading, yielding of the frame extended from the 1st story beam to the 2nd story beam at θ_2 = +1.0% (denoted as LS3), and to the 1st story column feet at θ_1 = +1.2% and θ_1 = -1.7% (denoted as LS4 and LS5, respectively). The peak IDRs experienced during this loading phase were θ_1 = -1.7% and θ_2 = +1.1%, which are within the limit of ±2% specified in GB 50011-2010 [14].

Under the VRE-level loading, the peak IDRs reached θ_1 = -2.7% and θ_2 = -1.3%. No new limit state and no strength degradation of the system were observed, but more extensive plasticity developed in the locations of earlier limit states. For the limit state of near collapse, the metric of inter-story drift is often used. For instance, the 4% limit is defined as the near collapse limit in Fahnestock et al. [35], and the 5% limit is used in Hsiao et al. [36]. By either standard, no collapse or near collapse was obtained in the test with the maximum inter-story drift below 4%, which indicated the possible good collapse-prevention performance of such systems even under the VRE-level hazard. After the VRE-level loading, a residual IDR of 0.11% was obtained at the 1st story while the residual deformation at the 2nd story was negligible. It is worth noting that due to the high uncertainty in earthquake excitations, the response under one ground motion record is not sufficient to conclude the residual deformation of such system. Results under more ground motion records are needed to conduct the statistical analysis to have more solid evaluation.

Under the quasi-static loading, no new limit state other than plasticity expansion in the frame developed until the IDRs approached +3%. When the IDR first reached +3%, slight bending occurred in the flange of beam B1 on the right side (denoted as LS6, see Fig. 12), and fracture initiated in the foot of column C1-L at the intersection between the column flange and the base rib (denoted as LS7). As shown in Figure 12, the fracture was induced by the plastic strain concentration at the intersection between the base rib and column flange. When IDR first reached -3%, slight bending was observed in the flange of column C1-L close to the column foot (denoted as LS8). After twelve cycles of low-cycle fatigue loading at the IDR of ±2%, the fracture in the column C1-L extended into the web (denoted as LS9), resulting in a 16% loss in $V_{C,1}$ and 8% loss in $V_{BRB\text{-}MF,1}$ at the IDR of +2% as compared with their corresponding maximum values at the same IDR, and the test was stopped. The fracture

is unlikely to be caused by the adoption of sliding gusset connections, because plastic hinges would develop at column feet at large drifts no matter sliding or welded gusset connections have been adopted. Moreover, the initiation and propagation of the fracture did not affect the hysteresis of BRBs. As shown in Fig. 11, all the BRBs still exhibited full, stable and repeatable hysteresis after 18 cycles of loading in the 2nd pseudo-static loading phase.

Throughout the test, no failure was observed in the beam-column-gusset regions, which validated the effectiveness of the sliding gusset connections and the damage-control design in preventing premature failure caused by the frame action as elaborated in the Introduction.

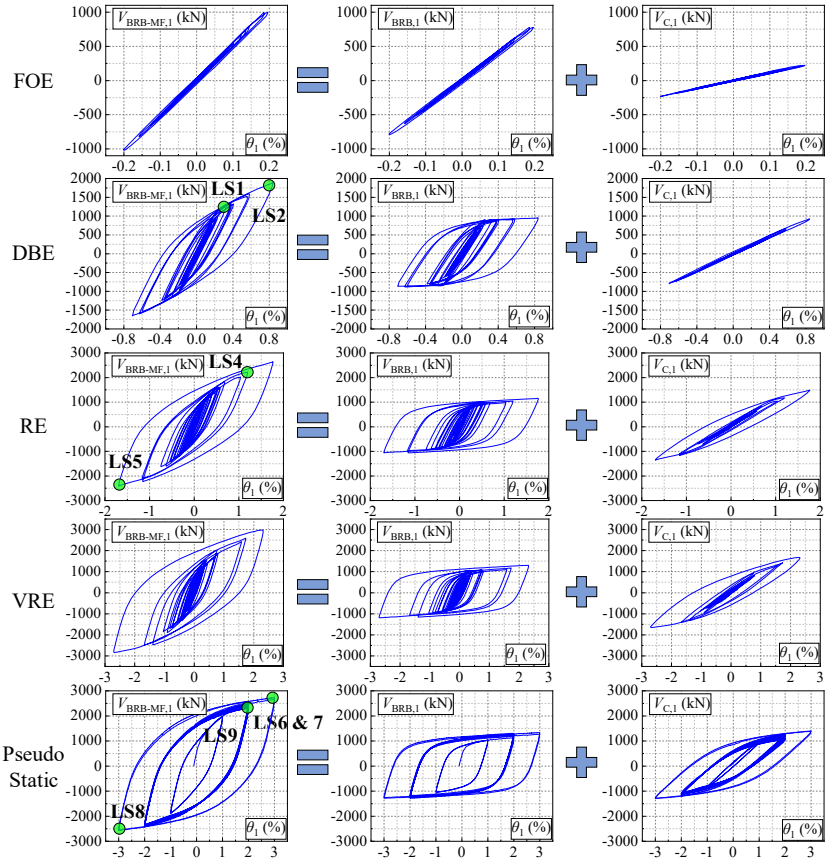

Figure 10 The story shear-IDR responses of the 1st story

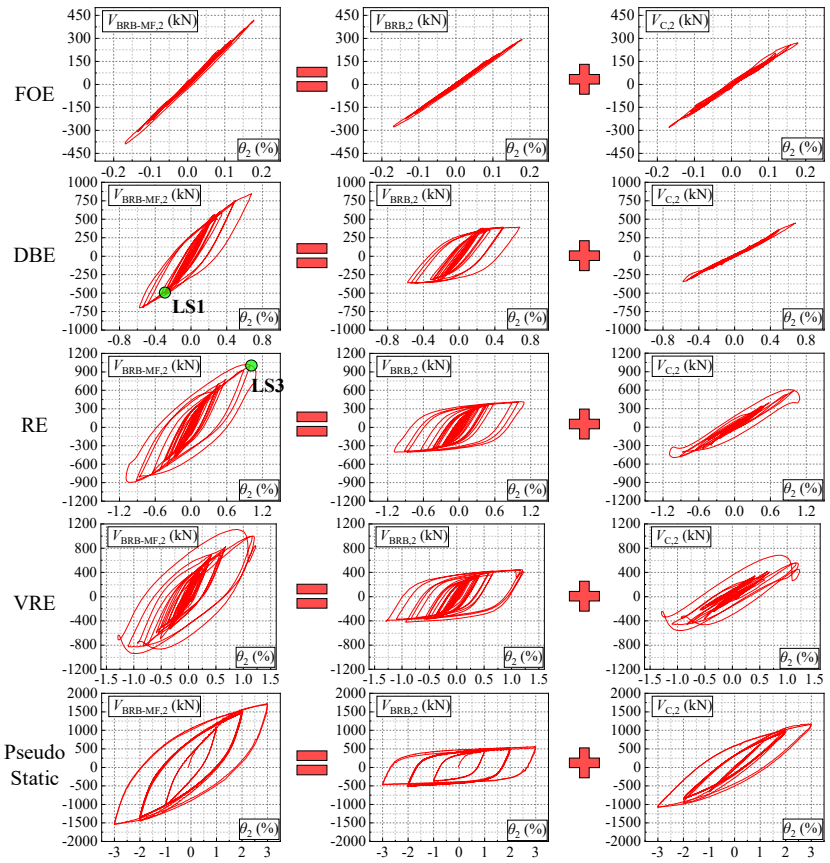

Figure 11 The story shear-IDR responses of the 2nd story

5.2 Performance of the moment frame

As evidenced from Figures 10 and 11, the MF contributed a significant portion of the lateral resistance for the system, which is consistent with the intention that the MF serves as one of the main lateral force-resisting parts in BRB-MFs. More importantly, the MF exhibited sufficient ductility to deform with the BRBs in a compatible manner up to the IDR of ±3%. Plastic hinges of the frame primarily formed in the intended positions, i.e. at the beam sections outside the gusset connection region and the column feet as shown in Figure 13, and no local buckling or fracture was found during the four-phase earthquake loadings. During the following quasi-static cyclic loading, only minor bending occurred in some of the beam and column plastic hinges; fracture did not initiate until the IDR reached +3% and developed at a slow rate.

The previous studies at the connection level [24,25] showed that when conventional welded gusset connections are used, the frame action, i.e., the beam-column joint opening and closing as shown in Figure 1, would result in severe plasticity in both the gusset plate and the frame. Particularly, the beam experienced severe plasticity concentration and significant local buckling outside the gusset tip region. In this test at the system level,

only minor bending was found in the beam flange at the IDR of 3% and no fracture was observed in the beam-column-gusset regions, which indicated the effectiveness of sliding gusset connections in reducing the negative frame action effect. To verify this conclusion at the system level, further study, specifically comparison with frames having welded gusset connections, is needed, which is ongoing by the authors.

Such performance of the MF verified that the design procedure presented in Section 3 was effective to control the plastic hinges to the desirable positions. In addition, the test results showed that the seismic detailing adopted, i.e., the transverse stiffeners in the expected plastic hinges, helped prevent premature local buckling at these positions, which is believed to have further improved the ductility of the MF.

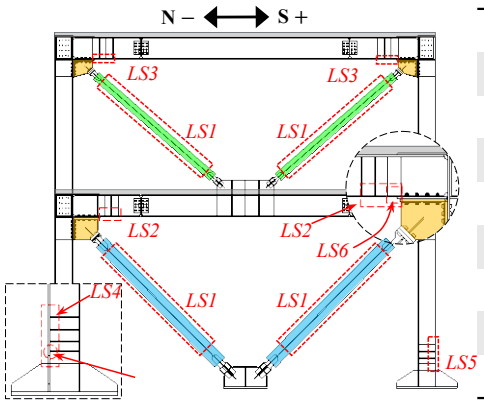

LS1	BRB yielding	θ_1 = +0.23% θ_2 = -0.23%	DBE
LS2	Yielding of lower flanges of beams B1	θ_1 = +0.8%	DBE
LS3	Yielding of lower flanges of beams B2	θ_2 = +1.0%	RE
LS4	Yielding of outside flange of C1-L	θ_1 = +1.2%	RE
LS5	Yielding of outside flange of C1-R	θ_1 = -1.7%	RE
LS6	Slight bending of beam lower flange	θ_1 = +3.0%	PS
LS7	Fracture initiation in the outside flange	θ_1 = +3.0%	PS
LS8	Slight bending of the column flange	θ_1 = -3.0%	PS
LS9	Fracture extension to the column web	After 12 cycles	PS

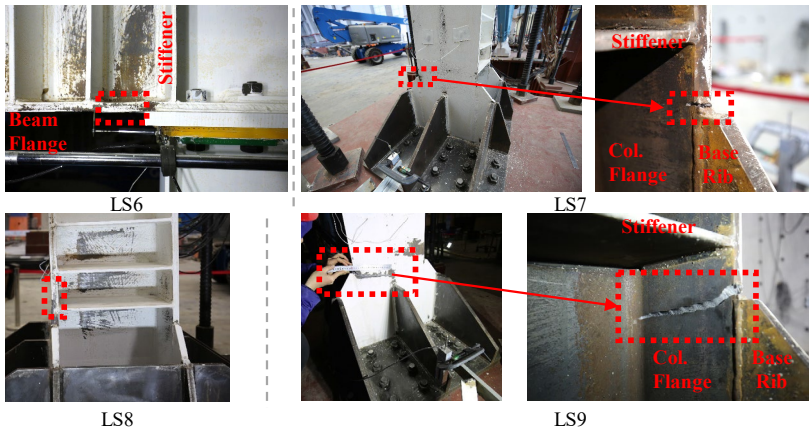

LS6 LS7 LS8 LS9

Figure 12 Position and summary of limit state (LS) evolution

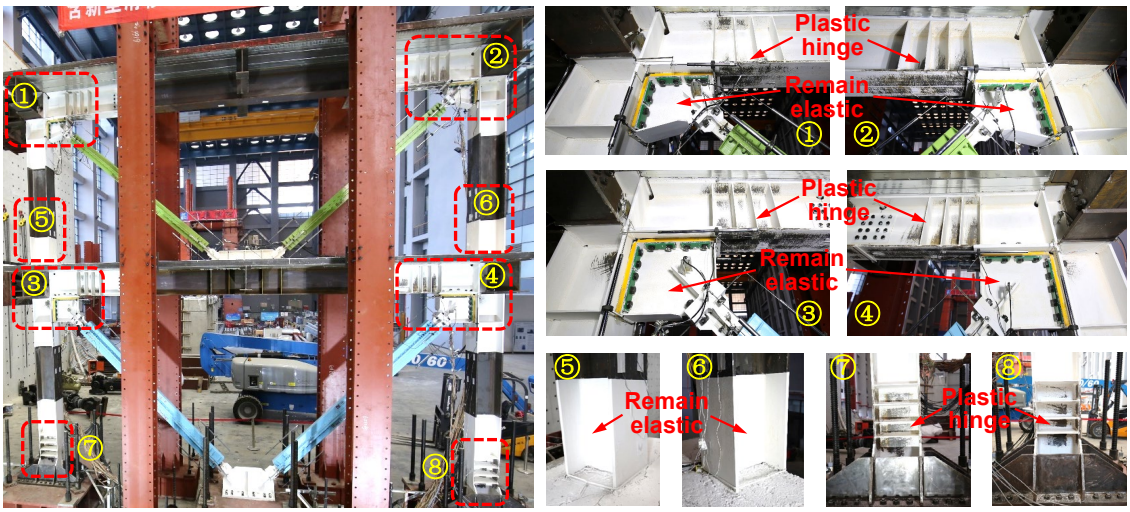

Figure 13 Damage of the moment frame at the end of the testing

Based on the strain gauge data and plain section assumption, the bending moments in the columns and beams were calculated. Figures 14 (a) and (b) show the moment diagram of the frame when the IDR first reached ±0.17% and ±2% during the pseudo static loading, which corresponded to the displacement amplitudes under FOE and the IDR limit under RE, respectively. As shown, the moment distribution in the MF was almost linear and asymmetric. The presence of sliding gusset connections seemed not to have affected the moment distribution in the frame, which indicates that sliding gusset connections could effectively release the frame-gusset interaction under both weak and strong earthquake loadings.

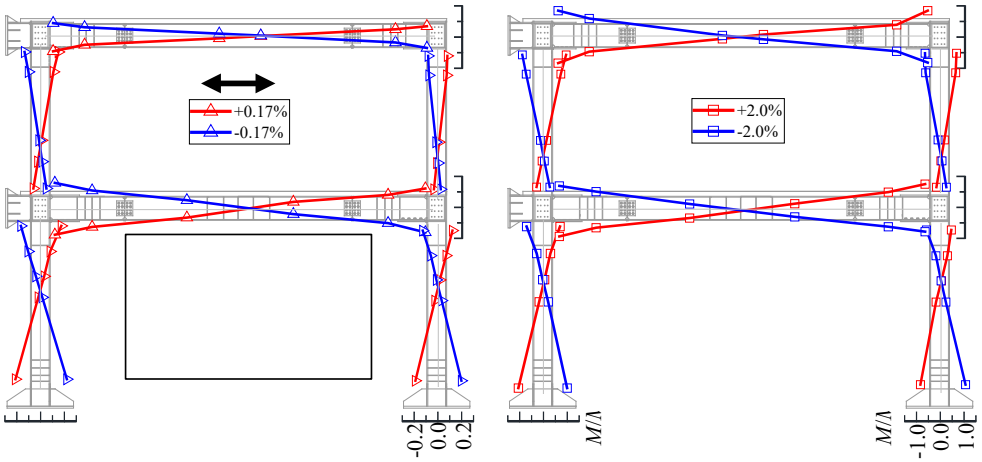

(a) (b)

Figure 14 Moment diagram of the frame: (a) at $\theta_1 = \theta_2 = \pm 0.17\%$; (b) at $\theta_1 = \theta_2 = \pm 2\%$

Based on the data collected by the strain rosettes on the panel zones, the maximum von Mises response was 299.6 MPa, well below the nominal yield strength of panel zone (345 MPa). This verifies the effectiveness of Ineq. (8) to maintain the elasticity of panel zone under VREs.

5.3 Performance of sliding gusset connections

5.3.1 Gusset plate interface stress

As evidenced from Figure 13, no instability or yielding was observed by visual inspection in the four sliding gusset plates throughout the tests. Based on the strain rosette data, the stress distributions (normal stress, shear stress, and the von Mises stress) along the gusset-to-end plate interfaces were plotted for the four gusset plates when θ_1 and θ_2 first reached ±3% during the pseudo-static loading, as shown in Figure 15. The results of the north side gusset plates (SG1-L and SG2-L) were mirrored about the vertical mid-plane of the frame and integrated with those of the south side ones (SG1-R and SG2-R) for better comparison.

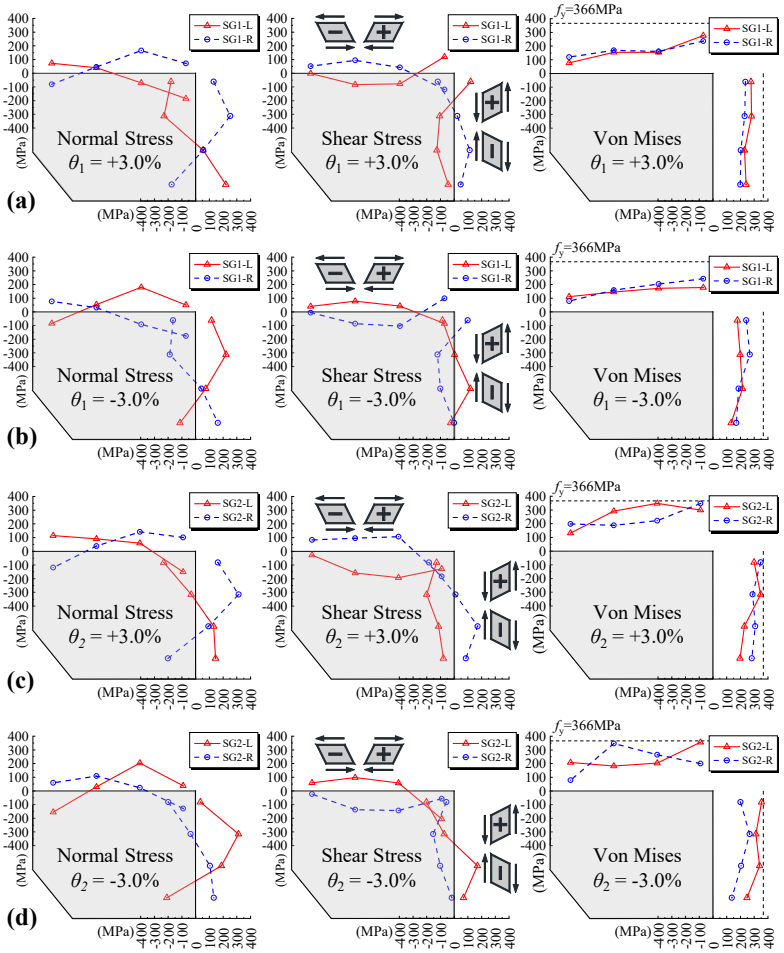

Figure 15 Gusset plate stress distribution: (a) θ_1 = +3.0%; (b) θ_1 = -3.0%; (c) θ_2 = +3.0%; (d) θ_2 = -3.0%

As for the stress composition, the magnitude of shear stresses was generally smaller than that of normal stresses, contrary to the case of the conventional welded gusset connections reported in Zhao et al. [24] where the shear stress governed. This is because the sliding mechanism released most shear restraint at the gusset-to-frame interfaces. Two patterns of stress direction were identified: (1) the direction of shear stress was mainly determined

by the relative movement at the gusset-to-frame interfaces, which can be well explained by the frictional forces when relative sliding occurred; (2) the normal stresses at the gusset tips were always in the opposite direction to the normal stresses at the gusset corner, which is mainly due to the tensile (clamping) forces at gusset tips imposed by the opening (closing) of the beam-to-column joint.

The magnitude of von Mises stresses showed that at $\theta_1 = \theta_2 = \pm 3\%$, the two sliding gusset plates in the 1st story (i.e. SG1-L and SG1-R) still remained elastic, and only minor localized yielding occurred near the gusset corner in the two sliding gusset plates in the 2nd story (i.e. SG2-L and SG2-R). This validated from system level that designing sliding gusset connections following the method in Section 3.2 in which only the brace action is considered is effective to keep the sliding gusset plates essentially elastic under reversed cyclic loading at large structural deformation levels.

5.3.2 Bolt tension force

The two bolts in SG1-R and the two bolts in SG2-R, for which the bolt tension forces were measured, are referred to as M24-1 and M24-2, and M20-1 and M20-2, respectively, with M24 and M20 indicating the nominal diameter of the bolts. Figure 16 shows the bolt axial force histories under the FOE-level loading. The four bolts remained elastic, and their pretension forces were almost unchanged after the loading. The result indicates that sliding gusset connections can maintain their functionality and there is no need to re-tighten or replace the high-strength bolts in the sliding gusset connection after FOE-level earthquakes.

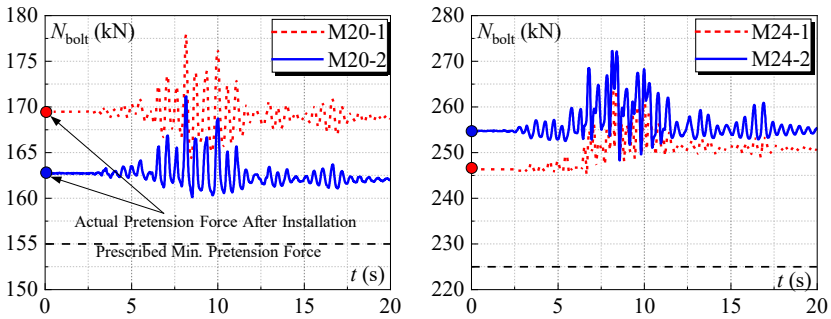

Figure 16 Bolt axial force histories under FOE-level loading

In Figure 17, the bolt axial force versus IDR responses under different loading phases were plotted. To evaluate the effectiveness of Ineq. (4) to ensure safety of the bolts, the nominal yield strength (N_y) and expected tensile strength (N_u=1.1 times the nominal tensile strength) of each bolt was plotted in grey dashed lines. In

general, the bolt axial forces tended to increase when sliding gusset connections was loaded in tension. Under the DBE-level loading, the four bolts remained elastic. At both the RE and VRE levels, the force in M24-1 exceeded the corresponding nominal yield strength while all the other 3 bolts remained elastic. During the quasi-static test, the bolts M24-1 and M20-2 experienced axial forces in excess of their corresponding nominal yield strength.

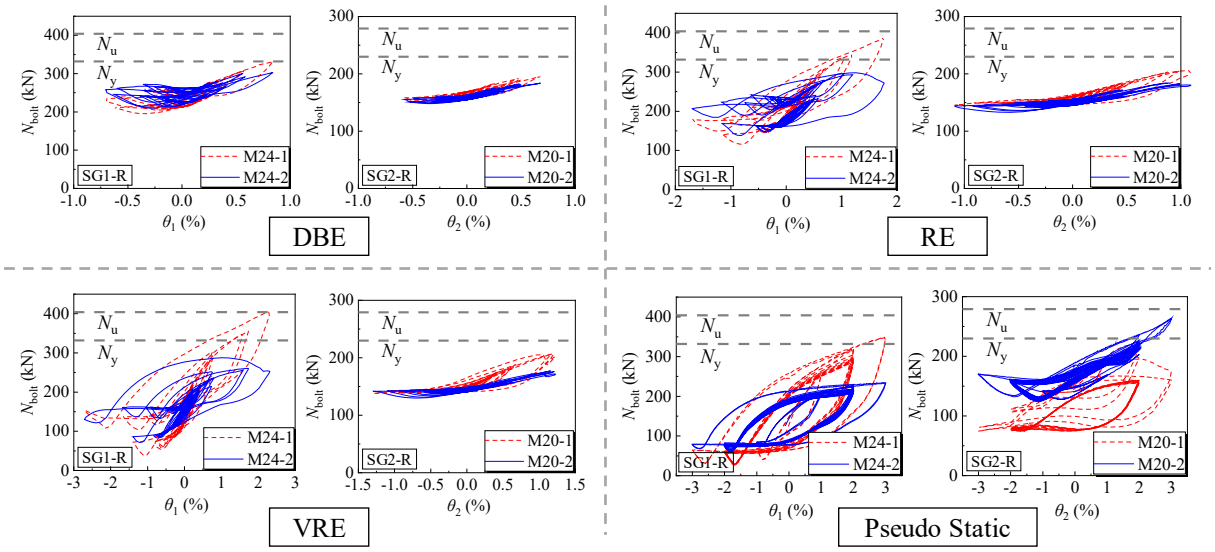

Figure 17 Bolt tensile force vs. inter-story drift ratio

It is noted that significant differences existed in the tensile forces of the two bolts in the same sliding gusset connection, especially at large structural deformation levels. This may be due to the existence of out-of-plane moment imposed on the bolt group that was possibly induced by initial geometric imperfections during construction process. Despite this, most of the bolts still remained elastic under the RE- and even VRE-level loading, and the tensile forces of all bolts fell below their expected tensile strengths. The safety of the bolts was also verified by the fact that no bolt rupture was observed throughout the tests.

5.3.3 Sliding deformations at the gusset-to-frame interfaces

Relative sliding deformations at the gusset-to-frame interfaces was observed and measured throughout the test. Figure 18(b) shows the relative sliding of SG1-R when θ_1 first reached $\pm 3\%$, with the sign defining as positive corresponding to shortening of flanges as denoted in Figure 18 (a).

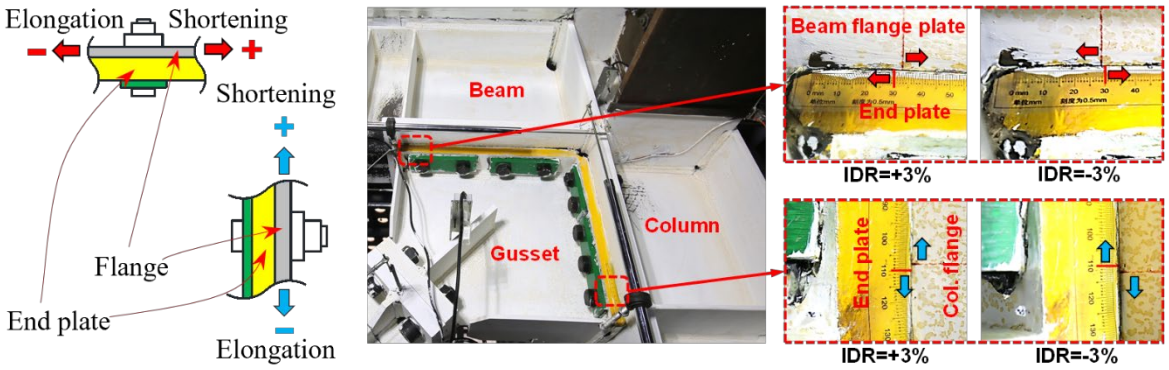

(a) (b)

Figure 18 Observed sliding deformations:(a) sign definition; (b) sliding of SG1-R at $\theta_1 = \pm 3\%$

Figure 19 shows the relative sliding deformations at the gusset-to-frame interfaces versus the IDR (δ-θ) responses. Sliding was activated from the FOE-level loading, although the structural deformation was small. The early sliding indicates that the sliding gusset connections can start to release the shear restraint at the gusset-to-frame interfaces under FOE. The magnitude of sliding increased with the IDR magnitude, and for each gusset connection the positive sliding was comparable in magnitudes to the negative ones at the same IDR level. The sliding at the gusset-to-beam interface was slightly larger than that at the gusset-to-column interface due to the formation of beam plastic hinging. Under the VRE-level loading, the maximum sliding occurred in SG1-R with a magnitude of 5.65 mm, corresponding to 1.2% the sliding interface length. This validates that the slotted hole length of 2% the sliding interface length recommended by Zhao et al. [25] is sufficient to accommodate the sliding under strong earthquakes.

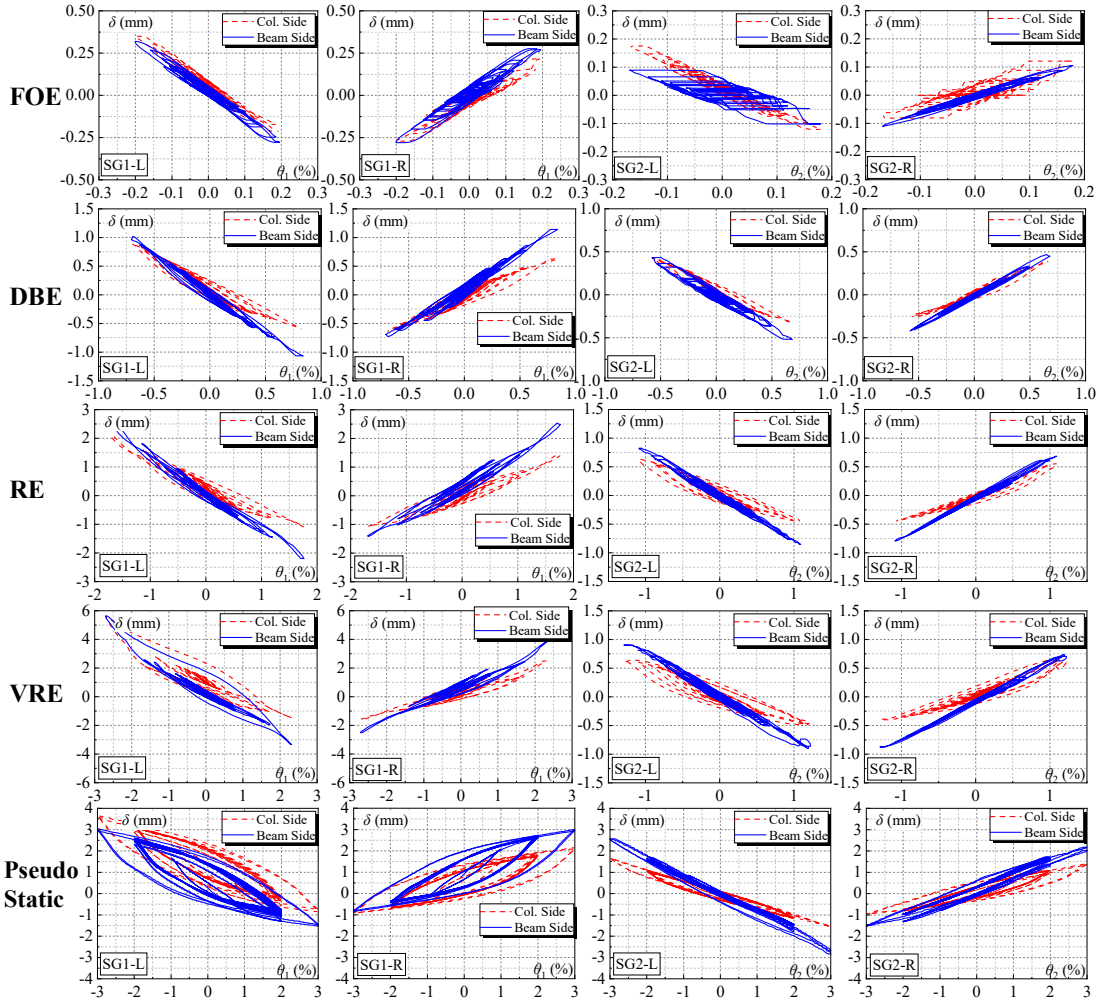

Figure 19 Sliding at the gusset-to-frame interfaces vs. inter-story drift ratios

5.4 Evaluation of performance compatibility between BRBs and MF

The previous research [24,25] revealed that sliding in the gusset connections may cause loss in BRB axial deformation under tension loading due to (1) formation of beam plastic hinge within the gusset region, (2) yielding of panel zone, or (3) insufficient bolt pretension force in the sliding gusset connection. But the axial deformation loss under compression loading of BRBs was negligible due to bearing between the gusset plate corner and frame corner. At a negative IDR (say -3%), the right BRB in one story would be under compression and its axial deformation was taken as the reference. At the positive IDR of the same magnitude (i.e., +3%), the same BRB would be under tension, and an axial deformation of a smaller value than the reference value was deemed to indicate the axial deformation loss. Figure 20 shows the axial deformations of BRB core plates at typical IDRs for BRB1-R and BRB2-R. As shown, the axial deformations under tension loading were generally smaller than those under compression loading at the same IDR, indicating the deformation loss as expected. However, the

level of deformation loss was low and negligible at various IDRs. For instance, the losses were 4.5% and 0.7% for BRB1-R and BRB2-R at the IDR of -3%, respectively. This indicates that by satisfying PO 1 to PO 5, the normal interaction at the frame-to-gusset interfaces were successfully reduced, and therefore axial deformation loss of BRBs under tension loading could be negligible. This is one of the crucial factors to develop the full potential of BRBs with the sliding gusset connections.

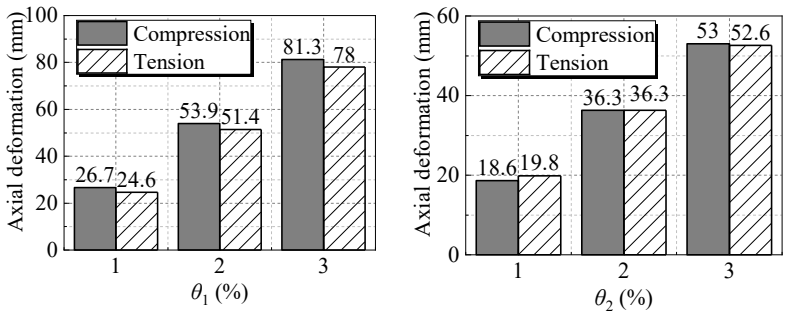

Figure 20 Axial deformation of BRBs at typical IDRs: (a) BRB1-R, (b) BRB2-R

Figures 10 and 11 show that the two story BRBs still exhibited symmetric, full and stable hysteretic responses during the pseudo static loading even after four levels of earthquake loading. To evaluate the fulfillment of BRB energy dissipation capacity, the cumulative plastic energy (CPE) index [37], defined as the sum of areas of the hysteretic loops divided by the strain energy of the BRB at the yield limit state, is adopted herein. As shown in Figure 21(a), the total CPE values of each BRB for all the loading phases exceeded 1100 and 710 for the 1st story and the 2nd story BRBs, respectively. The ductility index of BRBs, defined as the maximum IDR divided by the IDR corresponding to BRB yielding, reached 12 and 13 for the 1st story and the 2nd story BRBs, respectively. No fracture or buckling was observed in the BRBs during all the loading phases. This indicated that the BRB seismic performance had been fulfilled in the test BRB-MF. Two factors played a critical role in the successful fulfillment of the BRB potential: (1) the adoption of the sliding gusset connections reduced the frame action on the BRB connections and ensured reliable BRB axial force transfer to the frame; (2) the excellent compatible deformation capacity of the MF, which was designed following the damage-control method, helped maintain the integrity of the whole system under large deformation levels.

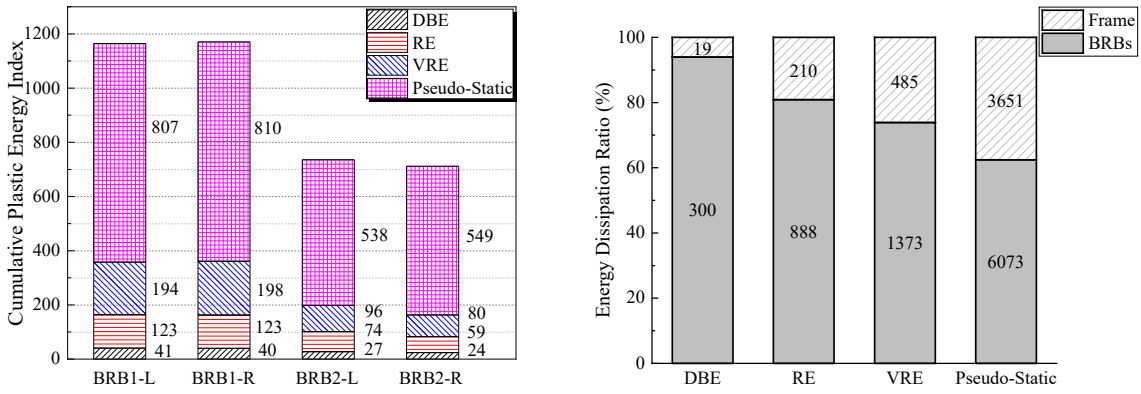

Figure 21 Energy dissipation: (a) CPE of BRBs, (b) comparison between BRB and frame (Unit: kNmm)

In addition to BRBs, the plastic hinges that formed in the MF also helped the structure to dissipate energy. In Figure 21(b), the energy dissipated by the BRBs and the frame was compared for all the loading phases except the FOE-level. As shown, BRBs dissipated most of the energy in all the loading phases, contributing 94%, 81%, and 74% of the total energy under the DBE-, RE-, and VRE-level loadings, respectively. This further confirms that by following the damage-control method, BRBs would work efficiently and serve as the main energy-dissipating elements in the BRB-MF system under earthquake loading.

6 Summary and conclusions

To ensure ductile seismic behavior of buckling-restrained braced moment frames (BRB-MFs), a damage-control design method was proposed and verified through experimental hybrid tests of a full-scale two-story BRB-MF in this study. Under the damage-control design framework, performance objectives of individual members were determined beforehand and corresponding design criteria were proposed accordingly. The damage-control design method was implemented for the BRB-MF of a two-story prototype building, which was experimentally studied by four hybrid tests and a pseudo static test. The key observations and conclusions are:

1. The tested BRB-MF exhibited excellent seismic performance with all the performance objectives achieved. Under the VRE-level loading, no damage was observed, and the system stood with no sign of imminent collapse. Even after the four-level hybrid earthquake loading, the system maintained a fair amount of ductility reserve.
2. By adopting the damage-control design procedure, the moment frame exhibited excellent ductility to have a compatible working relationship with BRBs. As intended, plasticity of the moment frame concentrated

in designated plastic hinges at beam sections outside sliding gusset connection regions and column feet. The transverse stiffeners prevented local buckling and strength degradation of plastic hinges, which effectively enhanced the ductility of the MF.

3. The moment distribution of the moment frame was nearly linear at both IDRs of ±0.17% and ±2%, which indicates that sliding gusset connections could effectively release the frame-to-gusset interaction under both small and strong earthquakes.
4. The von Mises stresses in the sliding gusset plates at IDRs of ±3% were essentially below the corresponding yield strength, which validated that the proposed connection level design procedure for sliding gusset connections is effective to keep sliding gusset plates stable and elastic in a realistic braced frame under strong earthquakes.
5. Monitoring of the axial forces in critical bolts of the sliding gusset connections revealed that the bolts remained elastic under the DBE-level loading, and the axial force of bolts still fell below their ultimate tensile strength even under VRE-level loading, demonstrating the adopted design method could guarantee safety of bolts under strong earthquakes.
6. Sliding in the sliding gusset connections was triggered under the FOE-level loading and increased in magnitude with the loading intensity, proving the ability of sliding gusset connections to release the frame-to-gusset interaction starting from small earthquakes. By adopting the proposed method, such sliding could be controlled to have little impact on the axial deformations of BRBs under tension loading.
7. By adopting the sliding gusset connections and the damage-control procedure, the integrity of the BRB-MF system was successfully maintained, and therefore BRBs could fulfill their energy dissipation potential and dissipate most of the energy induced to the system with negligible deformation loss.

Acknowledgments

This research is funded by the National Natural Science Foundation of China (Grant Nos. 51778244 and 52178481), Guangdong Basic and Applied Basic Research Foundation (Grant No. 2021B1515020057), and Guangdong Provincial Key Laboratory of Modern Civil Engineering Technology (Grant No. 2021B1212040003).

References

[1] Xu, L. H., Fan, X. W., & Li, Z. X. (2017). Cyclic behavior and failure mechanism of self‐centering energy dissipation braces with pre‐pressed combination disc springs. Earthquake Engineering & Structural Dynamics, 46(7), 1065-1080.

[2] Zhang, G., Xu, L. H., & Li, Z. X. (2021). Development and seismic retrofit of an innovative modular steel structure connection using symmetrical self-centering haunch braces. Engineering Structures, 229, 111671.

[3] Xu, L., Chen, P., & Li, Z. (2021). Development and validation of a versatile hysteretic model for pre-compressed self-centering buckling-restrained brace. Journal of Constructional Steel Research, 177, 106473.

[4] Zhang, Y., & Xu, L. (2022). Cyclic response of a self-centering RC wall with tension-compression-coupled disc spring devices. Engineering Structures, 250, 113404.

[5] Xu, L., Lin, Z., & Xie, X. (2022). Assembled self-centering energy dissipation braces and a force method-based model. Journal of Constructional Steel Research, 190, 107121.

[6] Black CJ, Makris N, Aiken ID. Component testing, seismic evaluation and characterization of buckling-restrained braces. Journal of Structural Engineering, ASCE 2004; 130(6): 880-894.

[7] Iwata M, Murai M. Buckling-restrained brace using steel mortar planks: performance evaluation as a hysteretic damper. Earthquake Engineering and Structural Dynamics 2006; 35: 1807-1826.

[8] Tremblay R, Bolduc P, Neville R, DeVall R. Seismic testing and performance of buckling-restrained bracing systems. Canadian Journal of Civil Engineering, 2006; 33: 183-198.

[9] Ding YK, Zhang YC, Zhao JX. Tests of hysteretic behavior for unbonded steel plate brace encased in reinforced concrete panel. Journal of Constructional Steel Research 2009; 65: 1160-1170.

[10] Palazzo G, López-Almansa F, Cahís X, Crisafulli F. A low-tech dissipative buckling restrained brace. Design, analysis, production and testing. Engineering Structures 2009; 31: 2152-2161.

[11] Wang CL, Usami T, Funayama J. Low-cycle fatigue testing of extruded aluminium alloy buckling-restrained braces. Engineering Structures 2013; 46: 294-301.

[12] Seyyed Ali Razavi Tabatabaei, Seyyed Rasoul Mirghaderi, Abdollah Hosseini. Experimental and numerical developing of reduced length buckling-restrained braces. Engineering Structures 2014; 77: 143-160.

[13] Yun Zhou, Chen Gong, Junxian Zhao, Genquan Zhong, Shiyu Tian. Strong-axis stability and seismic performance of perforated core plate buckling-restrained braces. Thin-Walled Structures. 2020, 156: 106997.

[14] GB 50011-2010. (2016). Code for seismic design of buildings, *China Building Technology Research Institute*. (in Chinese)

[15] Architectural Institute of Japan (AIJ). (2012). Recommendation for Design of Connections in Steel Structures, Tokyo. (in Japanese)

[16] Chou CC, Liu JH, Pham DH. (2012). Steel buckling-restrained braced frames with single and dual corner gusset connections: seismic tests and analyses. *Earthquake Engineering and Structural Dynamics* 2012; 41: 1137-1156.

[17] Lin PC, Tsai KC, Wu AC, et al. (2015). Seismic design and experiment of single and coupled corner gusset connections in a full-scale two-story buckling-restrained braced frame. *Earthquake Engineering and Structural Dynamics*, 44: 2177-2198.

[18] Lin PC, Tsai KC, Wu AC, et al. (2014). Seismic design and test of gusset connections for buckling-restrained braced frames. *Earthquake Engineering and Structural Dynamics*, 43: 565-587.

[19] Kishiki S, Uekusa M, Wada A. (2008). Experimental evaluation of structural behavior of steel member affected by the presence of gusset plate (Part 2). *Journal of Structural and Construction Engineering*, Architectural Institute of Japan,73: 2027-2036. (in Japanese)

[20] Kaneko K, Kasai K, Motoyui S, et al. (2008). Analysis of beam-column-gusset components in 5-story value-added frame. *Proceeding of the 14th World Conference on Earthquake Engineering*, Beijing, China.

[21] Jia MM, Lu DG, Guo LH, et al. (2014). Experimental research and cyclic behavior of buckling-restrained braced composite frame. *Journal of Constructional Steel Research*, 95: 90-105.

[22] Aiken ID, Mahin SA, Uriz P. (2002). Large-scale testing of buckling-restrained braced frames. *Proceeding of Japan Passive Control Symposium*, Tokyo Institute of Technology: Japan.

[23] Palmer KD, Christopulos AS, Lehman DE, et al. (2014). Experimental evaluation of cyclically loaded, large-scale, planar and 3-d buckling-restrained braced frames. *Journal of Constructional Steel Research*, 101: 415-425.

[24] Zhao, J., Chen, R., Wang, Z., & Pan, Y. (2018). Sliding corner gusset connections for improved buckling-restrained braced steel frame seismic performance: Subassemblage tests. *Engineering Structures*, 172, 644-662.

[25] Zhao, J., Li, Y., Wang, C., Chen, R., Yan, L., & Gong, C. (2021). Sliding corner gusset connections in concentrically braced frames using BRBs: Numerical analysis and practical design. *Engineering Structures*, 246, 113055.

[26] Mazzoni, S., McKenna, F., Scott, M. H., and Fenves, G. L. (2009). OpenSees command language manual, Univ. of California, Berkeley, Calif.

[27] PEER. (2021). "Pacific earthquake engineering research center PEER strong motion database." http://peer.berkeley.edu/peer_ground_motion_database.

[28] Chopra AK. (2012). Dynamics of structures: theory and applications to earthquake engineering. 4th ed. USA: Pearson Prentice Hall.

[29] Japanese Society of Steel Construction (JSSC). (2009). Fundamentals of steel structure design (4th ed), Gihodoshuppan, Tokyo. (in Japanse)

[30] JGJ 99-2015. (2016). Technical Specification for Steel Structure of Tall Building. *China Building Technology Research Institute*. (in Chinese)

[31] Zhao, J., Wu, B., Li, W., & Ou, J. (2014). Local buckling behavior of steel angle core members in buckling-restrained braces: cyclic tests, theoretical analysis, and design recommendations. *Engineering Structures*, 66, 129-145.

[32] Xu, G., Wu, B., Jia, D., Xu, X., & Yang, G. (2018). Quasi-static tests of RC columns under variable axial forces and rotations. Engineering Structures, 162, 60-71.

[33] Yang, G., Wu, B., Ou, G., Wang, Z., & Dyke, S. (2017). HyTest: platform for structural hybrid simulations with finite element model updating. Advances in Engineering Software, 112, 200-210.

[34] GB18306-2015. (2015). Seismic ground motion parameters zonation map of China. General Administration of Quality Supervision, Inspection, and Quarantine of China, *China Standards Press*. (in Chinese).

[35] Fahnestock, L. A., Sause, R., & Ricles, J. M. (2007). Seismic response and performance of buckling-restrained braced frames. *Journal of Structural Engineering*, 133(9), 1195-1204.

[36] Hsiao, P. C., Lehman, D. E., & Roeder, C. W. (2013). Evaluation of the response modification coefficient and collapse potential of special concentrically braced frames. *Earthquake engineering & structural dynamics*, 42(10), 1547-1564.

[37] Zhao, J., Wu, B., & Ou, J. (2011). A novel type of angle steel buckling-restrained brace: Cyclic behavior and failure mechanism. *Earthquake Engineering & Structural Dynamics*, 40(10), 1083-1102.